Radar-Based Breast Cancer Detection Using a Hemispherical Antenna Array—Experimental Results

Maciej Klemm, Ian J. Craddock, Jack A. Leendertz, Alan Preece, and Ralph Benjamin

***Abstract*—In this contribution, an ultrawideband (UWB) microwave system for breast cancer detection is presented. The system is based on a novel hemispherical real-aperture antenna array, which is employed in a multi-static radar-based detection system. The array consists of 16 UWB aperture-coupled stacked-patch antennas located on a section of a hemisphere. The radar system is designed to be used with realistic three-dimensional (3D) breast phantoms, which have been developed, as well as with real breast cancer patients during initial clinical trials. Images are formed using two different beamforming algorithms and the performance of these algorithms is firstly compared through numerical simulation. Experimental results for the same beamforming techniques are then presented, demonstrating the successful detection of 4 and 6 mm diameter spherical tumors in the curved breast phantom.**

***Index Terms*—Breast cancer detection, medical radar, ultrawideband (UWB).**

I. Introduction

X-RAY mammography is currently the most common technique used in breast cancer screening. It employs ionizing radiation, requires uncomfortable compression of the breast during the examination and is of limited value for younger women. These limitations of mammography have resulted in research into alternative methods for imaging breast cancer.

Microwave imaging is one of the more promising candidates and has attracted the interest of a number of research groups around the world. An excellent review of this topic can be found in [1]. As presented there, currently there are two main streams in microwave breast imaging: 1. microwave tomography, 2. radar-based imaging. Both approaches rely on a difference in the electrical properties of normal and malignant breast tissues.

In microwave tomography [2]–[4] the aim is to reconstruct the electrical profile of the breast, by solving a nonlinear and ill-posed inverse scattering problem. The tomographic systems presented so far operate as a narrowband devices in a lower gigahertz regime (up to 3 GHz). Recently a pilot study of electromagnetic tomographic breast imaging was conducted [5].

In radar-based imaging, the goal is to create a map of microwave scattering, arising from the contrast in dielectric properties within the breast. The radar approach originates from military and ground-penetrating applications and was proposed for breast cancer detection in the late nineties independently by Benjamin in 1996 [6], [7] and Hagness in 1998 [8]. In contrast to most proposed Tomographic systems the proposed Radar systems operate at higher frequencies (up to 10 GHz) and use a large bandwidth (as much as 8 GHz). Most of these radars therefore operate as ultrawideband (UWB) radars, where scattering information is obtained from transmission and reception of short UWB electromagnetic pulses. A big advantage of radar-based imaging over the tomographic imaging is its relatively simple and robust signal processing.

In this paper we present experimental results from a radar-based breast cancer detection system. Our UWB radar system uses a hemispherical real aperture antenna array and a realistic 3-D spherical breast phantom model with electrical properties similar to real breast tissues. Our experimental system was built in a such way that it can be used directly with real breast cancer patients (clinical trials have recently commenced).

To date there have been only a few experimental breast-imaging radar systems reported in the open literature [9]–[12]. The first experimental systems [9], [10] were validated based on phantom materials which only sought to represent the *contrast* in the real part of the permittivity of the breast. More realistic experiments were presented in [11], [12] where the phantom materials used more closely replicated the properties of breast tissues. It should be emphasized that losses are as important as dielectric constant when choosing phantom materials, because losses have a major impact on system bandwidth and the amplitude of the measured tumor response.

Unlike the other published work described above, our approach is different in being based on *multistatic* radar operation, originally proposed for breast cancer and land mine detection by Benjamin [7]. Compared to the monostatic approaches, a multistatic approach with a fully-populated antenna array enables far more data to be gathered.

In our first prototype [13] a planar antenna array was used for convenience, with all antennas printed on the same substrate. Encouraging experimental phantom results showed that the strength of the multistatic radar approach in this application. However the performance of the flat array is limited by the finite beamwidth of the antennas and, additionally, a planar arrangement does not conform well to the breast.

This contribution presents the second prototype of our multistatic radar, based on a new *hemispherical* antenna array. We use the same antennas as before, however they are manufactured on separate substrates and fed by coaxial cable. Additionally, each antenna is cavity-backed to eliminate undesired back-reflections.

Manuscript received August 03, 2007; revised December 11, 2008. Current version published June 03, 2009.

The authors are with the Centre for Communications Research, Department of Electrical and Electronic Engineering, University of Bristol, Bristol BS8 1UB, U.K. (e-mail: m.klemm@bristol.ac.uk).

Color versions of one or more of the figures in this paper are available online at http://ieeexplore.ieee.org.

Digital Object Identifier 10.1109/TAP.2009.2019856

Our experimental results were obtained using two different post-reception focusing algorithms. The first algorithm is a standard delay-and-sum (DAS) focusing, commonly used in landmine detection [14], [15], ultrasound [16] and microwave breast cancer imaging [17]. Although DAS has its advantages (e.g., simplicity), it provides limited performance in terms of image resolution and clutter rejection. These well-known limitations have been addressed by techniques such as microwave imaging via space-time (MIST)—this data-independent algorithm was shown in [10], [18] to outperform mono-static DAS, although *multi*-static DAS still outperforms *mono*-static MIST [19].

More recently Xie *et al.* [19], [20] proposed a new data-adaptive algorithm for breast cancer detection based on robust Capon beamforming (RCB) [24], [25]. We will refer to the data-adaptive algorithm as to MAMI, following [19]. Using full-wave FDTD simulations with idealized antennas (point sources), the authors showed that their new MAMI algorithm provides better performance than multistatic DAS and MIST. These interesting results motivated us to use MAMI as an alternative beamforming method. We used [19], [20] as a guide in developing a data-adaptive algorithm which could be used with our radar system. The main differences are that we do not use any mono-static data from our array, and we have to take into account real antenna effects. To the best of our knowledge, results from data-adaptive beamforming in breast cancer detection with real measured radar data have not been presented before.

In a multistatic array the monostatic paths comprise a small proportion of the available signals (e.g., in a 16 element array only 13%), these paths also suffer the greatest skin reflection. Furthermore, in a practical system they would require the use of a directional coupler in the measurement system and this contributes cost and complexity. For these reasons we do not perform any mono-static measurements in our radar system.

This contribution also presents for the first time:

- a performance comparison of DAS and modified MAMI beamforming algorithms in the presence of preprocessing errors (based on numerical simulations);
- comparison of DAS and modified MAMI based on real measured radar data;
- Microwave radar-based imaging system for breast cancer detection which has been used with real cancer patients.

The following section presents details of our system, including information about the UWB antenna, the design of the curved antenna array and the 3D hemispherical breast phantom. In Section III we describe the signal processing techniques used for focusing and image formation. Next, in Section IV using numerically synthesized radar data we compare performance of two beamforming techniques (described in Section III). Section V presents a method to extract the tumor response from measured data. The final part of the paper, Section VI, presents experimental results of phantom tumor detection.

II. UWB Hemispherical Antenna Array and Measurement Setup

A. Antenna Design

An aperture stacked-patch antenna was designed to be used for breast cancer imaging. It is a modified version of the antenna presented in [21] and in [22] where it was used in the planar array for breast imaging. For the conformal array, the antenna was redesigned. The final antenna design in presented in Fig. 1. While the size of two stacked patches was kept the same as in [21], the ground plane was substantially reduced (being now $23 \times 29\ \mathrm{mm}^2$). Additionally, as we learnt from the experience of using the planar array (see [22]) it is better to shield the antenna from the surrounding environment, therefore we added a cavity at the back of the antenna. The cavity has planar dimensions of $23 \times 29\ \mathrm{mm}^2$ and is 17-mm long. To absorb the back radiation of the antenna and avoid any resonances the cavity was lined with the broadband absorbing material (Eccosorb FGM-40 from Emerson & Cuming). On the front face of the antenna a short 5 mm metallic screen [see Fig. 1(a)] was included to decrease the coupling between adjacent array elements.

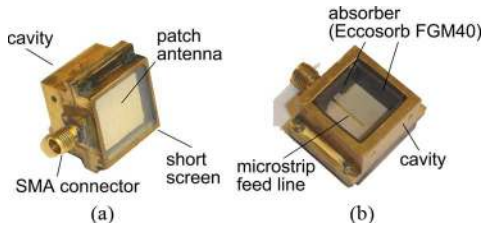

Fig. 1. Cavity backed aperture stacked patch antenna for breast imaging: (a) front side, (b) back side.

In Fig. 2 we present the antenna characteristics. We used a FDTD numerical solver during the design process and included the cavity, the absorber and the screen in the simulations. The comparison between simulated and measured antenna input match (S_{11}) is shown in Fig. 2(a), a good agreement was achieved and the antenna is well-matched between 4.5 and 10 GHz. Additionally, we performed a transmission measurement between two antennas (face-to-face) immersed in the matching liquid (described in the following paragraph). As an input pulse we chose a waveform presented in Fig. 2(b), which covers a frequency range between 4 and 9 GHz on -3 dB level. As described in [23], this type of pulse is suitable for time-domain analysis of microwave systems when performing measurements in the frequency-domain. The resulted pulse transmitted between our antennas is presented in Fig. 2(c). A distance between antennas was 6 cm. The transmitted pulse is clearly longer than the input pulse, due to the antenna's response but also due to the lossy (and dispersive) matching medium.

B. Conformal Antenna Array Design

Given the effort in designing and constructing a conformal hemispherical array, the intention from the outset was to design not only an array for laboratory use on a realistic, curved phantom, but also one that would serve as an initial clinical prototype. Approximately 20 female volunteers came forward from the University and the fit between their breasts and various plastic spherical sections was assessed with them lying in a prone position—the prone (face-down) position being felt to offer the best chance of the breast forming a gently and uniformly-curved shape. Following this assessment, the

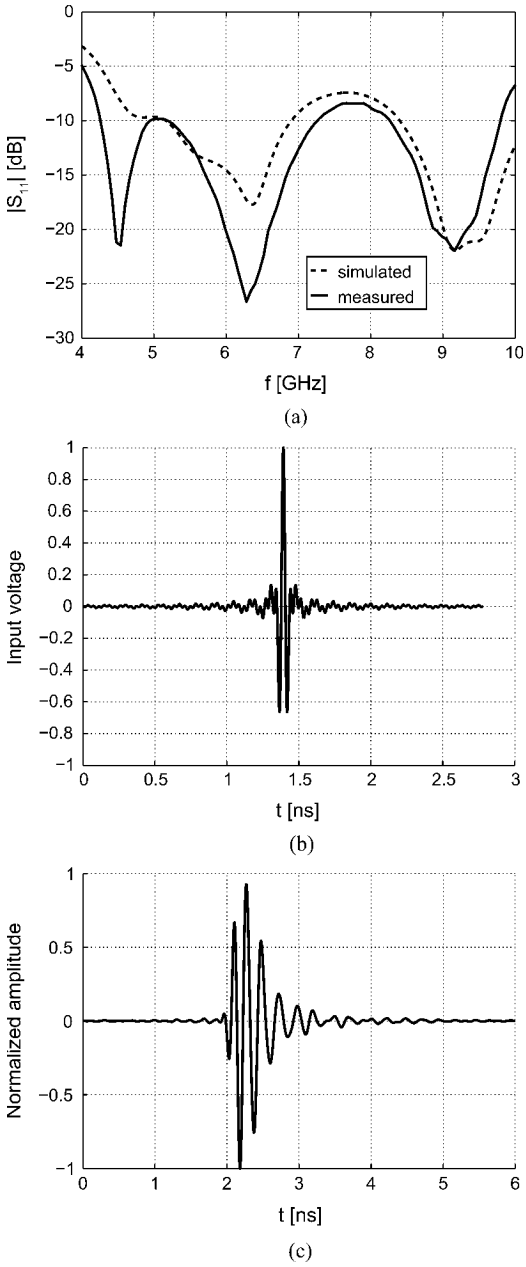

Fig. 2. Antenna characteristics: (a) simulated and measured input matching, (b) synthetic pulse used as antenna excitation, (c) pulse transmitted between 2 antennas (along boresight direction, 6 cm distance) immersed in the lossy matching liquid.

dimensions of the array were input into a 3D CAD model, along with the antenna elements and all supporting metalwork.

The resulting antenna array is formed around lower part of a 78-mm radius sphere, in four rows of four antennas. The side and top view of the array is shown in Fig. 3(a) and (b), respectively. The staggered arrangement of elements seen in Fig. 3(b) gives barely enough clearance for the cables and connectors, which pass between the elements of adjacent rows. The use of 3D CAD modelling was found to be vital, given the tight geometrical clearances and the difficulty in foreseeing, in a curved geometry, potential clashes between cables, connectors, antennas and supporting metalwork. The partly-constructed array is shown in Fig. 3(c).

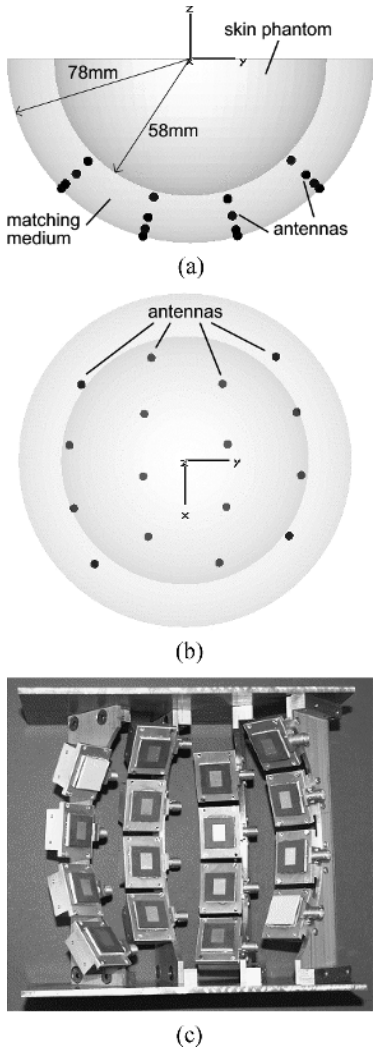

Fig. 3. Hemispherical antenna array and breast phantom configuration: (a) side view, (b) top view, (c) partly-constructed array.

In the measurement setup the array is connected with coaxial cables to a custom-built network of electromechanical switches, previously developed for the planar antenna array [13]. The bank of switches selects all possible pairs of antennas within the array and connects them in turn to a vector network analyzer (VNA), which performs the radar measurement in the frequency-domain (S_{21} in this case)—monostatic data (S_{11}) is not recorded. In a post-reception step all measured data are transformed into the time-domain. With sixteen antenna elements in the array, one hundred and twenty independent measurements (multistatic radar signals) are recorded. A computer controls both the VNA and the switch bank, and the measurement takes about 3 minutes to complete.

C. 3D Breast Phantom

For experimental testing we developed appropriate materials and a 3D breast phantom. As shown in Fig. 3(a), during the measurements the antennas are immersed in a matching liquid, to reduce reflections from the skin and for a more compact antenna design. We decided that the matching liquid would be the same as the material simulating properties of normal breast-fat,

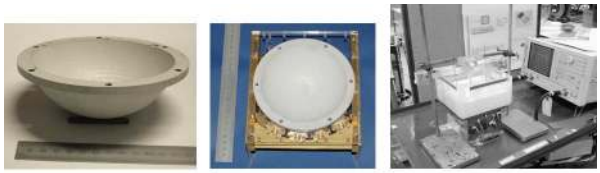

(a) (b) (c)

Fig. 4. Measurement setup: (a) curved skin phantom, (b) skin phantom fitted into the antenna array, (c) measurement setup for breast cancer detection experiments.

mainly for practical reasons (only one liquid required in manufacturing). The developed matching and normal breast tissue equivalent liquid [26] has a relative dielectric constant of about 9.5 and attenuation of $1.2\,\mathrm{dB/cm}$ at 6 GHz. This material is also dispersive (see [22] for frequency-dependent characteristics).

Next, a curved skin phantom was developed. The skin layer is 2-mm thick, it is a part of a 58-mm radius hemisphere [shown in Fig. 4(a)]. When skin phantom is fitted into the array, as presented in Fig. 4(b), it lies 20 mm above the antenna elements. This distance between antennas and breast provides a reasonable coverage of a breast by an antenna radiation pattern. Electrical parameters of the skin layer were chosen again according to the previously published data. The material is dispersive and at 6 GHz it has a relative dielectric constant of 30 and attenuation of $16\,\mathrm{dB/cm}$.

At last, a tumor phantom material with a relative dielectric constant close to 50 and conductivity $7\,\mathrm{S/m}$ (at 6 GHz) was developed. The contrast between dielectric properties of breast fat and tumor phantom materials is around 1:5. Recently published data in [27], based on a large clinical study, suggest that the contrast between healthy and malignant breast tissues might be lower. The complete measurement setup is presented in Fig. 4(c).

III. Focusing Algorithms

To obtain the 3D image of the scattered energy, we employ post-reception synthetic focusing. As described above, in this contribution we employ two distinct focusing methods. The first is based on the classical delay-and-sum (DAS) beamforming. The second method is a data-adaptive focusing algorithm, based on the robust Capon beamforming (RCB).

A. Preprocessing (Equalization)

Before applying either focusing algorithm we have to perform a preprocessing step. This process aims at equalization of scattered tumor responses for different antenna pairs. Ideal preprocessing would result in all received pulses being of the same shape, amplitude and perfectly time-aligned. In our preprocessing the following steps are performed: 1. extraction of the tumor response from measured data (described in detail in Section V), 2. equalization of tissue losses, 3. equalization of radial spread of the spherical wavefront.

Although in our experiments there is frequency-dependence of the tissue losses and of the antenna radiation patterns, for simplicity we do not compensate for that dependence in our processing.

B. Delay-and-Sum Algorithm

Delay-and-sum (DAS) beamforming is a basic and well-known method [16], [28], [29]. First we perform the preprocessing steps described above. Next, appropriate time-delays for all received signals are computed. The time-delay τ_{ij} for the $i\mathrm{th}$ transmitting and $j\mathrm{th}$ receiving antenna is calculated based on the positions of the two antennas, the position of the focal point r as well as an estimate of average wave propagation speed, which in our case is simply assumed to be constant across the band.

During the focusing, the focal point moves from one position to another within the breast, resulting in spatial beamforming. At each location all time-shifted responses are coherently summed and integrated. Integration is performed on the windowed signal, the length of the integration window is chosen according to the system bandwidth. Due to the antenna effects and dispersion, the integration window we utilize following coherent summation is 50 percent longer than the duration of the synthetic input pulse [shown in Fig. 2(b)] and equals 0.55 ns. We have investigated the dependence of the window length on focusing quality and this value gave best results.

A three-dimensional (3D) map of scattered energy is formed in this way. The main advantage of DAS algorithm is its simplicity, robustness and short computation time.

C. Data-Adaptive Beamforming

The second imaging algorithm we use is based on a robust Capon beamforming (RCB) [24]. Unlike DAS (or MIST), RCB can be classified as a data-adaptive (data-dependant) algorithm. It accounts for some uncertainties during preprocessing steps, e.g., nonideal time-delays, or errors in amplitude compensation.

The discussion here is based on [19] but with some additional comments and steps in the mathematics provided for clarity and completeness. Also after Xie *et al.* [19] we will refer to the data-adaptive algorithm as MAMI. The following notation is used: lowercase font for scalars, bold lowercase for vectors, bold uppercase for matrices.

The data-adaptive algorithm (MAMI) assumes that the preprocessed and times-aligned backscattered tumor response can be described as

$$\mathbf{y}_i(t) = \mathbf{s}(t)x_i(t) + \mathbf{n}_i(t);\ i = 1, \ldots, M-1; \quad \mathbf{y}_i(t) \in R^{M-1\times 1}. \tag{1}$$

M is a number of antennas used for focusing at a given focal point (not a number of antennas in an array as in [20]), scalar $x_i(t)$ is the true backscattered tumor response, $\mathbf{n}_i(t)$ represents the additive noise and interference (including remaining undesired reflections), $\mathbf{s}(t)$ is the so-called array steering vector. In our algorithm vector $\mathbf{y}_i(t)$ has a dimension $(M-1)\times 1$, not $M\times 1$ as in [19], because we do not use the mono-static signal.

$\mathbf{y}_i(t) = [y_{i,1}(t), \ldots, y_{i,i-1}(t), y_{i,i+1}(t), \ldots, y_{i,M-1}(t)]^T$ is the preprocessed signal vector, where $y_{i,j}(t)$ represents the multistatic array response for the $i\mathrm{th}$ transmitting (Tx) antenna and $j\mathrm{th}$ receiving (Rx) antenna. Note that $\mathbf{s}(t)$ would ideally be equal to a unitary vector $\mathbf{1}_{M-1\times 1}$, since equalization and time-shifting have already been applied. The signal model (1) required by RCB, assumes that the steering vector $\mathbf{s}$ depends

only on time, and the tumor response x depends on i (Tx antenna), but not on j (Rx antenna). While these assumptions are certainly not entirely true, the algorithm still performs well, as illustrated by the results in the following sections.

We denote the sampled signal model (1) by $y(k)$. It can be expressed as

$$y(k)=\mathbf{w}^*(k)\mathbf{y}_i(k)=\mathbf{w}^*(k)\mathbf{s}(k)x_i(k)+\mathbf{w}^*(k)\mathbf{n}_i(k) \quad (2)$$

where $\mathbf{w}$ is a vector of weights, introduced to account for the steering vector errors, $(\cdot)^*$ denotes the conjugate transpose.

In standard Capon beamforming (SCB) the goal is to minimize $\mathbf{w}^*\mathbf{n}_i(t)$ and make $\mathbf{w}^*\mathbf{s}(t) = 1$. Equivalently this objective can be stated as [30]: minimize $\mathbf{w}^*\mathbf{R}_n\mathbf{w}$, subject to $\mathbf{w}^*\mathbf{s}(t) = 1$, where $\mathbf{R}_n = \mathbf{E}(\mathbf{n}\mathbf{n}^*)$ is a covariance matrix and E denotes the expected value. This SCB formulation provides good results when the steering vector is known. The weight vector in SCB problem is then derived as

$$\mathbf{w}(t) = \frac{\mathbf{R}_n^{-1}(t)\mathbf{s}(t)}{\mathbf{s}(t)^*\mathbf{R}_n^{-1}(t)\mathbf{s}(t)}. \quad (3)$$

However, in the presence of steering vector errors, SCB can give worse results than simple DAS beamforming. To improve the performance of SCB when the steering vector is not known, RCB makes explicit use of an uncertainty of the steering vector. RCB assumes that the true steering vector $\mathbf{s}(t)$ is:

$$||\mathbf{s}(t) - \bar{\mathbf{s}}(t)||^2 \leq \epsilon \quad (4)$$

where $\bar{\mathbf{s}}(t) = [1, \ldots, 1]^T$ is the assumed steering vector, and ϵ describes the error in $\mathbf{s}(t)$.

In practical applications of Capon beamforming (SCB, RCB) there is usually no prior information about the noise ($\mathbf{R}_v$), therefore an estimate of the covariance matrix derived from recently received array output samples (including both signal and noise) is used. In our case this new covariance matrix has the following form:

$$\begin{aligned}\mathbf{R}_Y(t) &= \frac{1}{M}\mathbf{Y}(t)\mathbf{Y}(t)^* \\ \mathbf{Y}(t) &= [\mathbf{y}_1(t), \ldots, \mathbf{y}_{M-1}(t)] \\ \mathbf{Y}(t) &\in R^{M-1\times M-1}.\end{aligned} \quad (5)$$

Comparing to [19], $\mathbf{Y}(t)$ has smaller dimension and is asymmetrical. Additionally we need to take into account the finite beamwidth of practical antennas—to do this, we only allow signals from antennas seeing a given focal point within a limited solid angle to be included in the covariance matrix. This helps ensure that only signals with an adequate signal quality will contribute to the response. The covariance matrix will therefore have a different size in different focal locations. This effect is not considered in any of the [19], [20] papers, because authors used idealized point sources as antennas in their simulations. We also noted that using our real measured data, a larger value of ϵ (steering vector error) needs to be employed for stable results, compared to the values reported in [19].

As shown in [24] the problem can now be reduced to the quadratic optimization problem

$$\min \mathbf{s}^T(t)\mathbf{R}_Y(t)\mathbf{s}(t), \text{ subject to } ||\mathbf{s}(t)-\bar{\mathbf{s}}(t)||^2 \leq \epsilon. \quad (6)$$

Additionally, we need to assume that $\epsilon < ||\bar{\mathbf{s}}(t)||$, to exclude the trivial solution $\mathbf{s}(t) = 0$. The problem (6) can be solved using the Lagrange multiplier method [25], [30]

$$\hat{\mathbf{s}}(t) = \bar{\mathbf{s}}(t) - [\mathbf{I} - \lambda\hat{\mathbf{R}}_Y(t)]^{-1}\bar{\mathbf{s}} \quad (7)$$

where $\lambda \geq 0$ is a real-valued Lagrange multiplier.

Next, following the steps presented in [20 Eq. (17)–(22)], the final form of the RCB weight vector $\mathbf{w}_{RCB}(t)$ can be found. It requires eigendecomposition of the covariance matrix and the solution of a nonlinear equation. The resulted RCB weight vector $\mathbf{w}_{RCB}(t)$ has the following form shown in (8) at the bottom of the page.

In our case of the multistatic radar operation, the above presented RCB procedure needs to performed in two steps [20]. The first step is performed as presented above. After obtaining the weight vector (from 8), the beamformer output can be written as:

$$\hat{\mathbf{x}}(t) = [\mathbf{w}_{RCB}(t)\mathbf{Y}(t)]^T, \quad \hat{\mathbf{x}}(t) \in R^{M-1\times 1}. \quad (9)$$

Note here that $t = [t_1, \ldots, t_N] \in T_{int}$, where T_{int} is the time window used in the integration of the DAS algorithm. Therefore, we perform RCB for each time sample, to obtain the complete waveform estimate $\hat{\mathbf{x}}$. In the second step, we use the calculated $M-1$ waveforms ($\hat{\mathbf{x}}$), to estimate the backscattered energy at a given focal point. $\hat{\mathbf{x}}$ can be seen as the snapshot from the $M-1$ element array and can be described in a following form:

$$\hat{\mathbf{x}}(t) = \mathbf{s}_s x_s(t) + \mathbf{n}_s(t), \quad t = 0, \ldots, N-1. \quad (10)$$

Clearly (10) is analogous to (1), allowing the use of RCB again to estimate $x_s(t)$. Unlike the first step, RCB needs to performed

$$\mathbf{w}_{RCB}(t) = \frac{||\hat{\mathbf{s}}(t)||}{\sqrt{M}} \frac{[\mathbf{R}_Y^{-1}(t) + \frac{1}{\lambda}\mathbf{I}]^{-1}\,\hat{\mathbf{s}}(t)}{\hat{\mathbf{s}}^T(t)\,[\mathbf{R}_Y^{-1}(t) + \frac{1}{\lambda}\mathbf{I}]^{-1}\,\mathbf{R}_Y^{-1}(t)\,[\mathbf{R}_Y^{-1}(t) + \frac{1}{\lambda}\mathbf{I}]^{-1}\,\hat{\mathbf{s}}(t)}. \quad (8)$$

only once now. The covariance matrix is composed using samples of $\hat{\mathbf{x}}(t)$ in the following way:

$$\mathbf{R}_s = \sum_{t=0}^{N} \hat{\mathbf{x}}(t)\hat{\mathbf{x}}^T(t). \tag{11}$$

Based on that created covariance matrix, we perform the same steps of RCB as described in the first part (6)–(9), to obtain the estimate of the weighted output of the array: $\hat{x}_s(t) = \mathbf{w}^*_{RCB2}\ \hat{\mathbf{x}}(t)$. The backscattered energy for a given focal point r_0 can be finally calculated as

$$E(r_0) = \sum_{t=0}^{N-1} \hat{x}_s^2(t). \tag{12}$$

IV. Simulation Results

In this section we investigate the degradation of results from DAS and MAMI due to inaccuracies in calculation of time shifts during the data preprocessing steps. This is important, since the propagation velocity in the breast will vary between individuals and within each breast, hence the time-alignment process can only ever be approximate.

To do this, we used FDTD to numerically generate a tumor response for a 6 mm tumor, 20 mm behind the skin, at two different locations: $P1$ (x = 12, y = 12, z = −12) and $P2$ (x = −21, y = 21, z = −33). Knowing the tumor location, permittivity of the breast and antenna positions, the appropriate time-delays for each antenna pair were calculated to include pulses scattered by the tumor in transient data (120 signals). These ideally calculated time-delays provide the best case for coherent focusing since all signals are perfectly time-aligned.

In order to investigate the nonideal focusing case, we introduced random variations to the time delays (according to a normal distribution with mean zero and variable standard deviation (σ)). In each data set, we have assumed a value of the standard deviation of the delay, and then for each one of the 120 radar signals a random delay was calculated (using the $randn$ Matlab function). Several realizations for the same σ were created, as obviously each realization provides unique delays, which are also randomly distributed between different paths (antenna pairs). It should be noted that during focusing different paths make different contributions, depending on their position in the array, and hence the affect of a variation in a time delay will depend on the particular path it arises in.

Signal to clutter ($\mathrm{S/C}$) ratio, defined as the ratio between energy of the strongest tumor response to the strongest clutter energy within a single 3-D image, was used as a focusing quality measure.

In Fig. 5 we present signal-to-clutter ratio results for standard deviation values of up to 7% (in 1% steps). In the figure the discrete results (circles for DAS, crosses for MAMI) represent the single realization of random delays for a given σ. Based on this discrete data the $\mathrm{S/C}$ curves were calculated using least-square fitting.

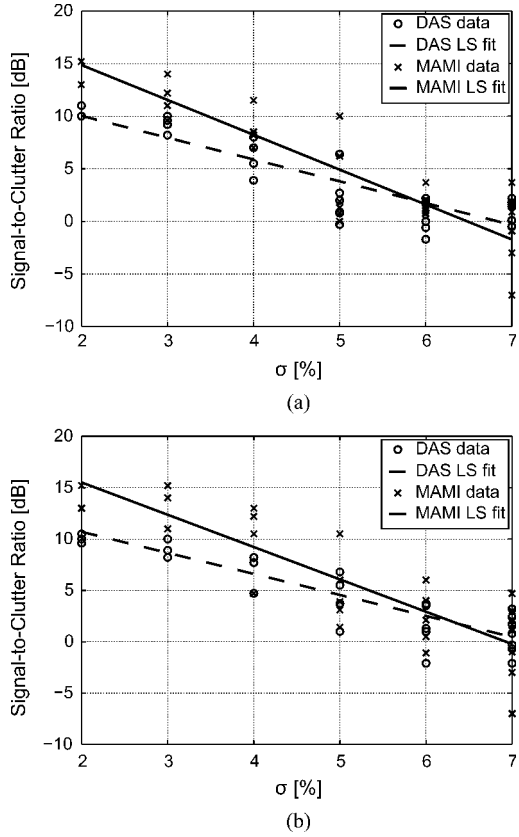

Fig. 5. Signal-to-clutter ratio [dB] for varying standard deviation of delay error values. (a) Software tumor located at x = 12, y = 12, z = −12. (b) Software tumor located at x = −21, y = 21, z = −33.

These numerical results show that the MAMI beamforming outperforms DAS for lower σ values, providing more than 5 dB gain in $\mathrm{S/C}$ for σ of up to 2%. However, as time-delay error increases, both curves get closer to each other, and around $\sigma = 6\%$ we can observe that they cross.

In Fig. 6, we present a focusing result example (2D slice through the real tumor location) for tumor position $P1$, and delay error of $\sigma = 7\%$, where DAS provides generally better results than MAMI. We can observe that for DAS [Fig. 6(a)] in spite of a significant level of clutter present in a large area of the image, the tumor can still be identified. For MAMI beamforming [Fig. 6(b)] there is generally lower background clutter, however the true tumor response (see figure) is not dominant in the focused image. In this case the clutter "target" would be more probably identified as the main scattering object.

Based on the results presented above we concluded that MAMI based on [24] is relatively efficient in suppressing the background clutter and improves the focusing quality. But it does not improve the tumor detection, and when the preprocessing errors are above certain level the simple DAS provides better results. This is important in real-life situations where experimental errors and variations between patients will inevitably degrade the quality of the data.

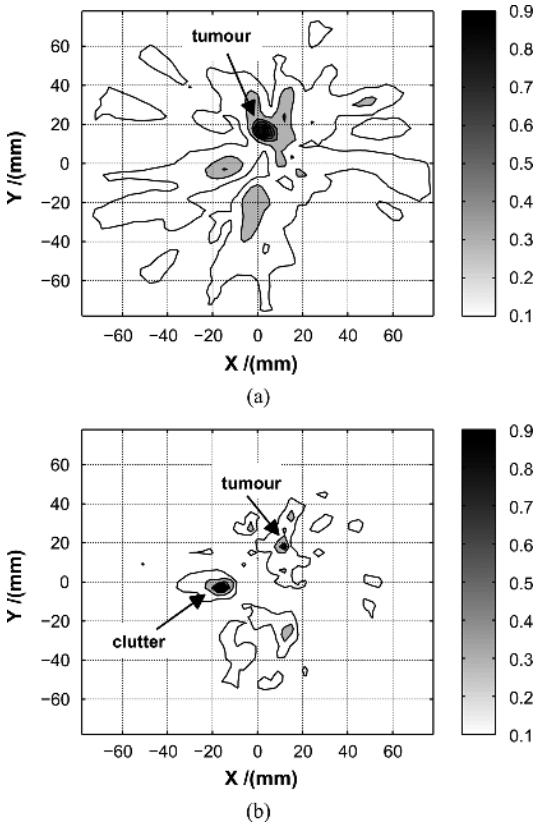

Fig. 6. 2D focused images of the tumor located $P1$ ($\mathrm{x} = 12, \mathrm{y} = 12, \mathrm{z} = -12$) for the case of delays error of $\sigma = 7\%$. (a) Results for DAS focusing, (b) results for adaptive focusing. Contour plots show signal energy on a linear scale, normalized to maximum in the 3D volume, values below 0.1 rendered as white.

V. Extraction of the Tumor Response—Array Rotation

Above we have presented the preprocessing step and the focusing algorithms. However, before these can be applied, the tumor response must be extracted from measured data. Measured data contains the tumor response, as well as additional undesired signals (antenna coupling, reflections from the skin, reflections from mechanical parts of the array). To subtract all unwanted signals, we physically rotate the antenna array. This target displacement method is commonly used in radar cross-section measurements [31], [32], to subtract all unwanted signals (in [33] authors use a 4-element planar antenna array for breast imaging. They minimize the coupling between antennas by using a lossy substrate, and use array rotation, with 4 positions, only to increase the number of measured data).

Rotation gives us two sets of measured data, in which undesired signals such as antenna coupling, or skin reflections are almost identical and appear at the same time position, therefore they can be eliminated. In contrast, a tumor response will appear at different time position in these two measured sets (unless it is on the axis of rotation). Applicability of this technique will depend on the homogeneity of the breast within a given angle defined by rotation. We therefore assume that within the angle of array rotation: (a) distance between antennas and skin remains unchanged, (b) skin properties and thickness is the same, (c) normal breast tissue properties do not change.

Depending on the angle of rotation and quality of data, we can observe one or two scatterers in the focused images. Examples for a tumor located at two different location are presented in Figs. 7 and 8 below. For each location we present the tumor detected at two positions (P1, P2) using ideal background subtraction (with and without tumor), and the same tumor detected using offset rotation (array rotated by 10 deg, from position P1 to P2). After investigations concerning the angle of rotation, we found out that 10 degree rotation provides satisfactory performance. A more detailed analysis of this issue is beyond the scope of this contribution. Background subtraction can be treated as the ideal way of extracting tumor response. However, it can not be used with real patients.

In Fig. 7 the example of the detected 6 mm tumor is shown. Four measurements using our experimental setup were performed to obtain presented results: M1- background measurement without tumor, M2- measurement when tumor in position P1, M3- measurement when tumor in position P2 (after 10 deg array rotation), M4- second background measurement after taking out tumor. Using this set of measurements we are able to detect tumor: (a) located in position P1 [see Fig. 7(a)], using background subtraction (using measurements M1 and M2), (b) located in position P2 [see Fig. 7(b)], using background subtraction (using M3 and M4), (c) located in position P1/P2 [see Fig. 7(c)], using rotation subtraction (M2 and M3).

As we can see in Fig. 7(c) the subtraction based on array rotation provides good results, and the tumor is clearly detected at positions almost exactly matching those from the ideal background subtraction [Fig. 7(a) and (b)]. The offset subtraction resulted in this case in two scattering centres of similar amplitude, what we will call in the following a *twin-target*. Slightly different results are presented in Fig. 8(c), showing detection of a larger (10 mm) tumor. In this case we observe that the subtraction based on rotation results in one scattering center in position P1 being stronger than in position P2 (but still visible).

VI. Experimental Detection Results

In this section we present experimental results of tumor detection using two focusing algorithms described above. In all examples presented below, tumor responses were extracted from measured data using rotation subtraction. To prove that using our radar system we are capable of detecting small tumors (at least in phantoms), we present examples of 6 and 4 mm spherical tumors located at two different positions: P1: $\mathrm{x} = 20$, $\mathrm{y} = 0$, $\mathrm{z} = -10$; P2: $\mathrm{x} = -20$, $\mathrm{y} = -15$, $\mathrm{z} = -10$ (dimensions in [mm]). The skin contour is visible for clarity on 2D and 3D images.

A. 6 mm Tumors

In Figs. 9 and 10, we present detected 6-mm tumors located at position P1 and P2, respectively. Each figure presents results when using DAS and MAMI beamforming, for comparison. A three-dimensional (3D) scattering energy image (showing -1.5 dB energy contour), as well as a horizontal cut containing the maximum focused energy are presented. All images show normalized (to the maximum energy within a 3D imaged volume) results.

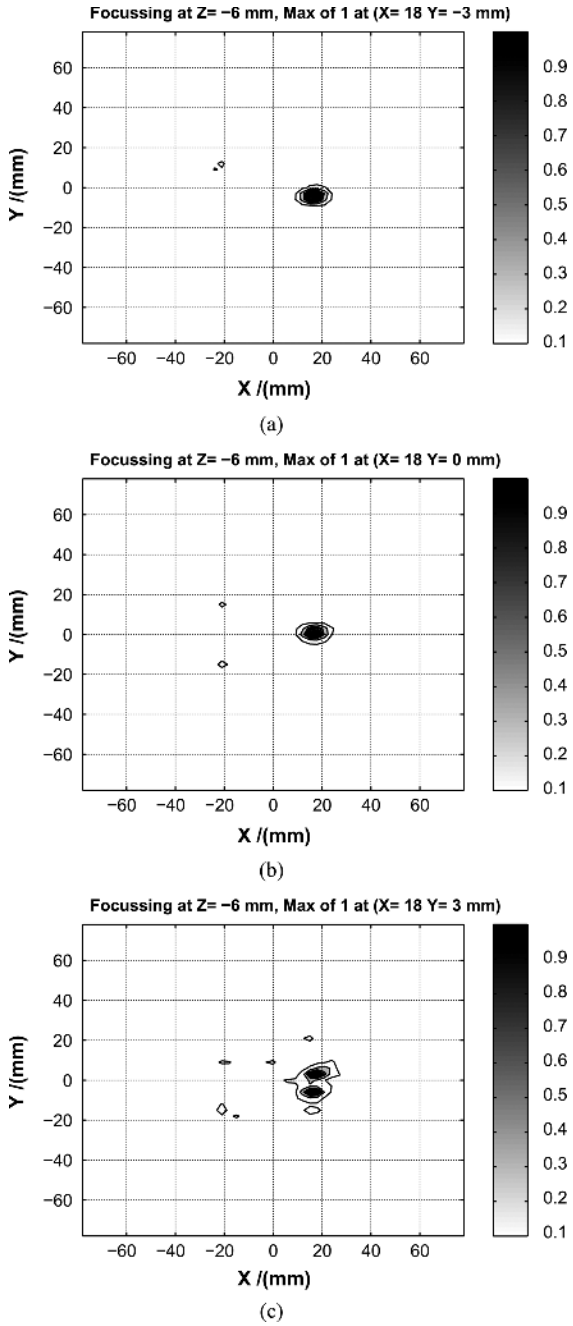

Fig. 7. 2D images presenting detection of 6 mm tumor using different techniques to extract tumor response: (a) background subtraction when tumor is in position P1, (b) background subtraction when tumor is in position P2, (c) offset rotation from P1 to P2 (10 deg). DAS used for focusing. Contour plots show signal energy on a linear scale, normalized to maximum in the 3D volume, values below 0.1 rendered as white.

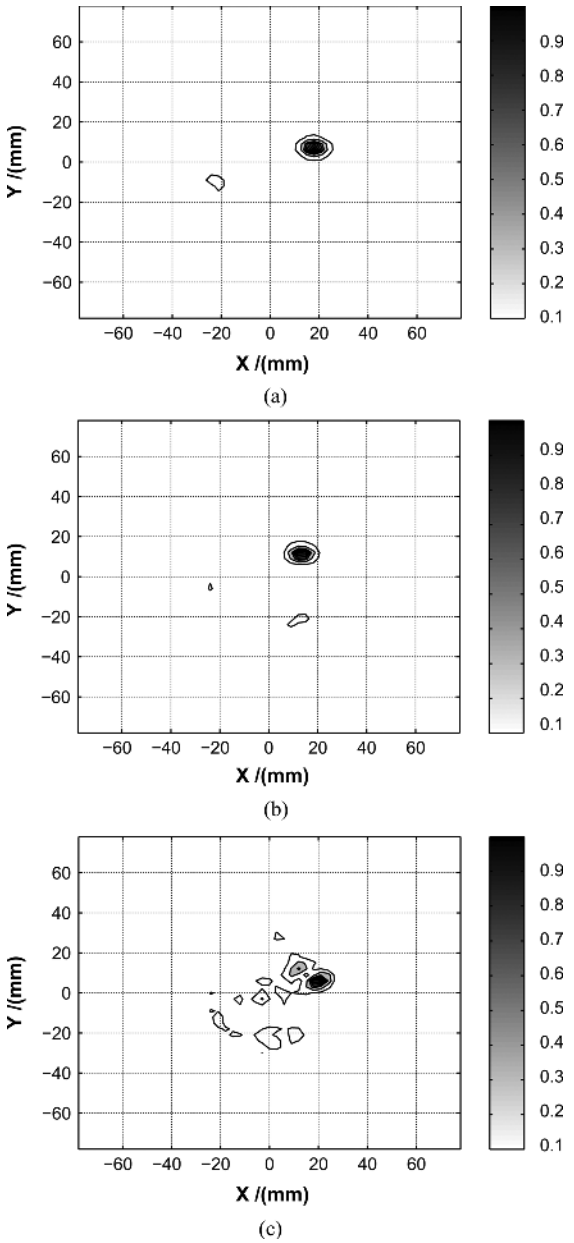

Fig. 8. 2D images presenting detection of 10 mm tumor using different techniques to extract tumor response: (a) background subtraction when tumor is in position P1, (b) background subtraction when tumor is in position P2, (c) offset rotation from P1 to P2 (10 deg). DAS used for focusing. Contour plots show signal energy on a linear scale, normalized to maximum in the 3D volume, values below 0.1 rendered as white. Results are based on real measurements using our radar system.

As we can see, both algorithms clearly indicate the detected tumors at the correct positions. Images are clear, with little clutter content, though slightly higher for DAS. Results of imaging for position P2 (Fig. 10) present the advantage of MAMI algorithm in terms of focusing sharpness and background clutter reduction. Due to array rotation a *twin-target* is observed, indicating the good quality of the measured tumor response. Quantitative results of signal-to-clutter ratio will be presented below (Section VI-C).

B. 4 mm Tumors

For the same tumor location as above we conducted detection experiments with 4 mm spherical tumor phantoms. Imaging results are presented in Figs. 11 and 12 for locations P1 and P2, respectively. We can observe that results for DAS beamforming are clearly poorer, compared to the 6 mm tumor size. Strong clutter is present on 3D as well as 2D images. It might be difficult to recognize the tumor position without *a priori* knowledge.

Significantly better results are obtained when using MAMI beamforming for image formation (Fig. 11(c) and (d) for location P1 and Fig. 12(c) and (d) for location P2). We can see that

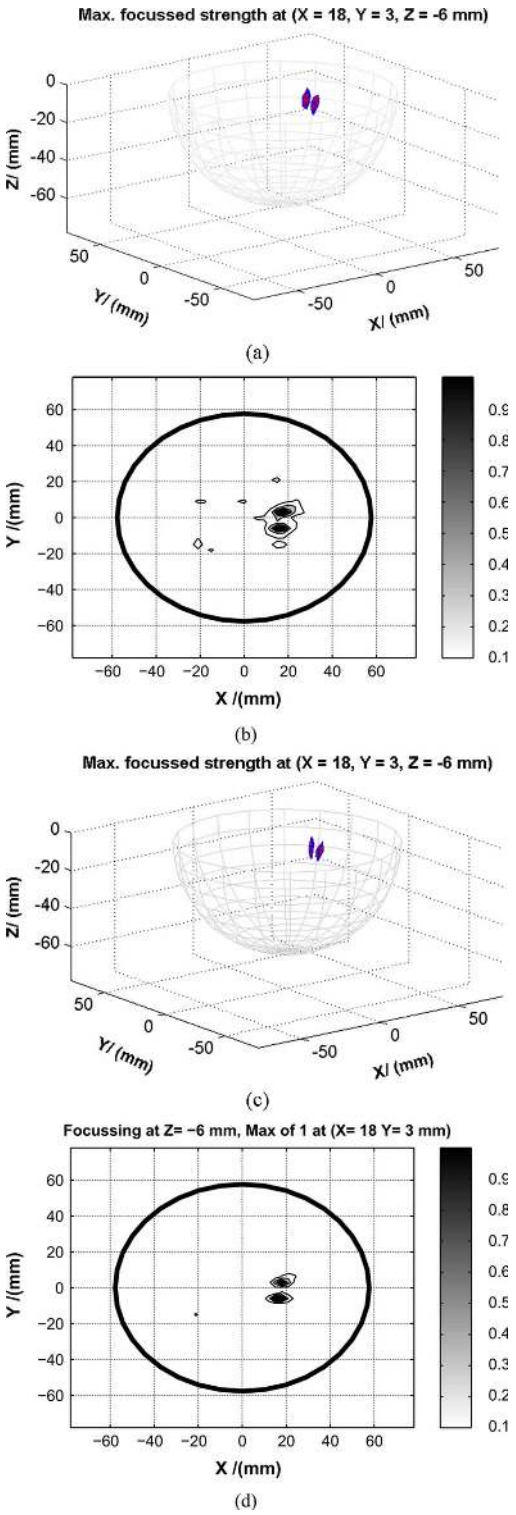

Fig. 9. 6 mm tumor located at the position $\mathrm{x} = 20, \mathrm{y} = 0, \mathrm{z} = -10$ (P1). Offset rotation (10 deg) used to extract tumor response. (a) DAS results-3D, (b) DAS results-2D, (c) *MAMI*-3D, (d) *MAMI*-2D. 3D figures present -1.5 dB contour map. 2D contour plots show signal energy on a linear scale, normalized to maximum in the 3D volume, values below 0.1 rendered as white.

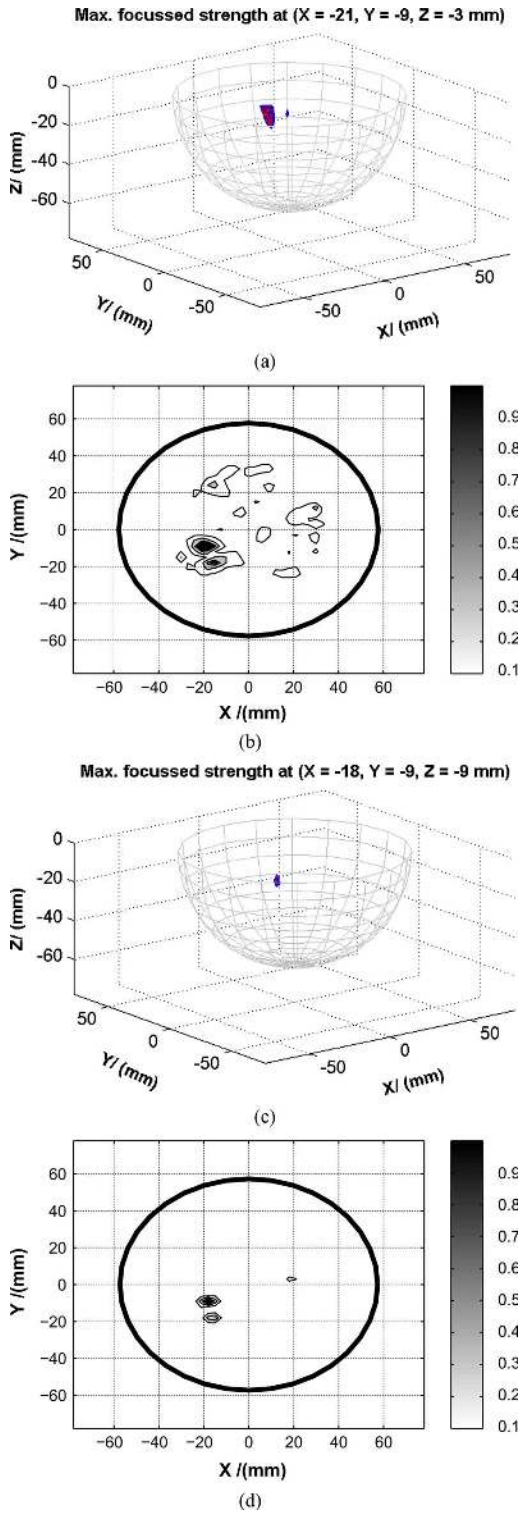

Fig. 10. 6 mm tumor located at the position $\mathrm{x} = -20, \mathrm{y} = -15, \mathrm{z} = -10$ (P2). Offset rotation (10 deg) used to extract tumor response. (a) DAS results-3D, (b) DAS results-2D, (c) MAMI-3D, (d) MAMI-2D. 3D figures present -1.5 dB contour map. 2D contour plots show signal energy on a linear scale, normalized to maximum in the 3D volume, values below 0.1 rendered as white.

the clutter is greatly reduced, resulting in relatively clearer 3D and 2D images. Unlike for 6 mm tumors, this time we do not observe the *twin-target* , which indicates the overall performance degradation.

C. Signal-to-Clutter Ratio

One possible quantitative measure of the detection quality is a signal-to-clutter ratio ($\mathrm{S/C}$). As before we define the signal-to-clutter as in the ratio between energy of the strongest tumor response to the strongest clutter energy, within a single 3-D image.

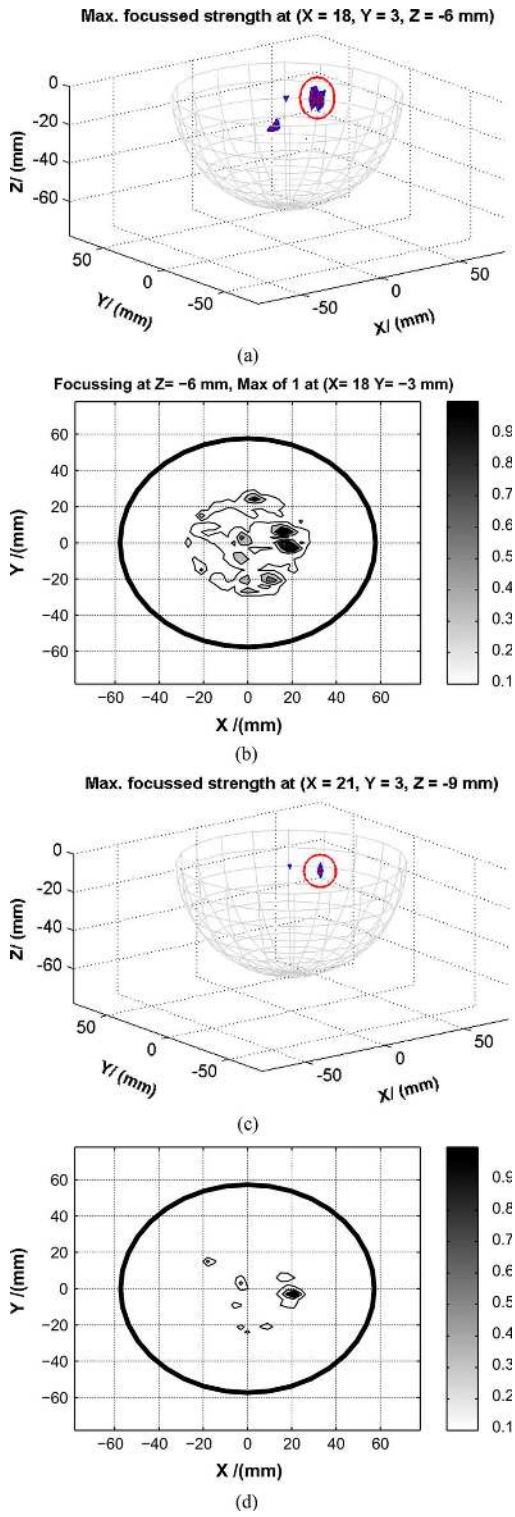

Fig. 11. 4 mm tumor located at the position $\mathrm{x} = 20, \mathrm{y} = 0, \mathrm{z} = -10$ (P1). Offset rotation (10 deg) used to extract tumor response. (a) DAS results-3D, (b) DAS results-2D, (c) MAMI-3D, (d) MAMI-2D. 3D figures present -1.5 dB contour map. 2D contour plots show signal energy on a linear scale, normalized to maximum in the 3D volume, values below 0.1 rendered as white.

For the imaging experiments with 6 mm and 4 mm tumors presented above, we have listed the corresponding S/C values (in [decibels]) in Table I.

TABLE I
SIGNAL TO CLUTTER RATIO [dB]

	DAS		*MAMI*	
	P1	P2	P1	P2
6 mm	6.2	3.8	7.1	8.2
4 mm	0.45	0.7	1.2	2.9

P1: x=20, y=0, z=-10
P2: x=-20, y=-15, z=-10

Results show that in all experiments the S/C for MAMI beamforming are higher than for DAS. Results of S/C of 7.1 dB for location P1 and 8.2 dB for location P2 when imaging 6 mm tumor are pleasing. MAMI gives improvement over DAS of 0.9 and 4.4 dB for positions P1 and P2. For 4 mm tumors the absolute S/C values are lower and range from 0.45 to 2.9 dB, when both beamforming algorithms are considered. The S/C for MAMI is higher by 0.75 and 2.2 dB for location P1 and P2, respectively. Improvement over DAS is slightly smaller than for 6 mm tumors, however, due to the lower absolute values of S/C, although visually the improvement of imaging with MAMI is more pronounced (e.g., compare results in Fig. 12).

VII. DISCUSSION

In previous sections we have presented the experimental characterization of the multistatic radar-based system for breast cancer detection. Experiments were based on a simplified spherical breast phantom, with homogeneous tissue mimicking materials and relatively light dielectric contrast between tumor and surrounding breast tissue. Recently published data on electromagnetic (EM) properties of breast tissues [27] suggest that the contrast might be significantly lower and also that the breast interior is more inhomogeneous that indicated in previously published reports [34]–[36]. Our work has been done before findings from [27] were known, we therefore shall discuss their potential impact on a performance of our system and microwave breast imaging in general.

Results the most recent study mentioned above show that the EM contrast between cancer and normal fatty tissue was as high as 10:1 but was no more than about 1.1:1 when malignant properties were compared to normal glandular and fibroconnective tissue in the breast. It suggests that results of microwave imaging will highly depend on a specific breast structure. We can envision two main scenarios:

1. Tumor can be embedded in a large dense tissue (glandular or fibroconnective). If the contrast between tumor and this tissue will be indeed 1.1:1, it would a major challenge for microwave radar-based imaging.
2. Tumor will be surrounded by the fatty tissue (relatively high contrast scenario), but there will be some portion of the breast composed of the tissue with properties similar to that of the tumor (e.g., fibro-glandular tissue).

Then, it will highly depend on a specific scenario: the relative positions between the tumor and fibro-glandular tissue, shape and size of the glandular tissues. Generally, tumor detection will depend on a clutter generated by the glandular tissues within the breast. It is possible that both, the tumor and glandular tissue will be visible on the focused images.

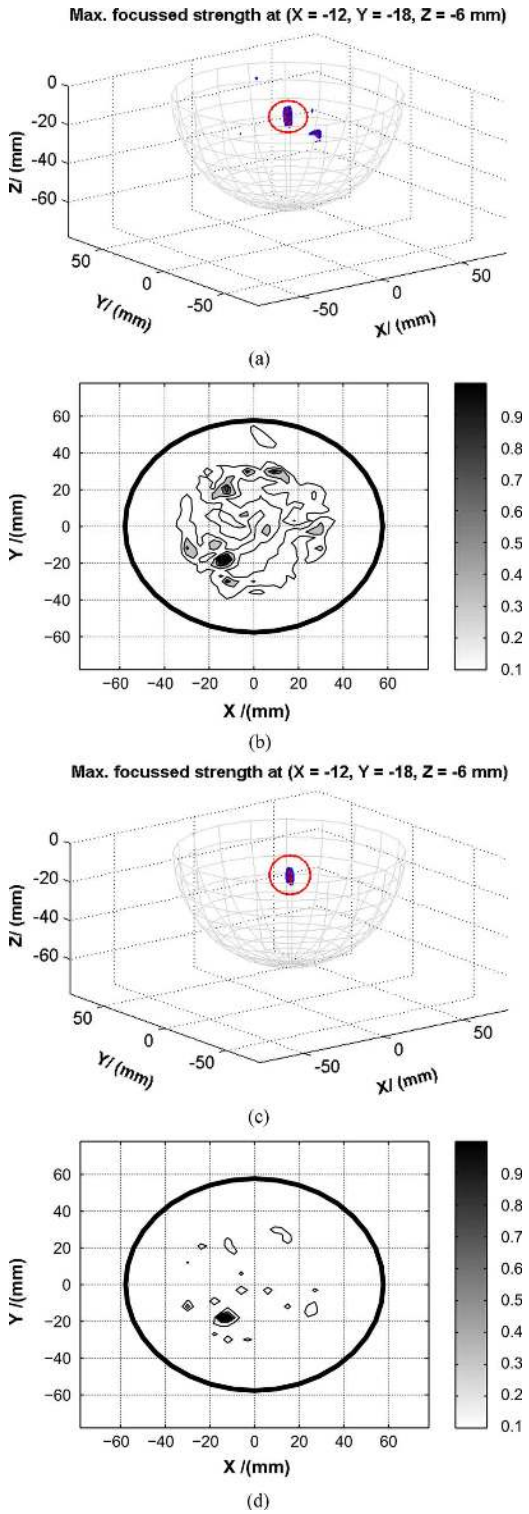

Fig. 12. 4 mm tumor located at the position $x = -20, y = -15, z = -10$ (P2). Offset rotation (10 deg) used to extract tumor response. (a) DAS results-3D, (b) DAS results-2D, (c) MAMI-3D, (d) MAMI-2D. 3D figures present -1.5 dB contour map. 2D contour plots show signal energy on a linear scale, normalized to maximum in the 3D volume, values below 0.1 rendered as white.

Issues discussed above show that there is a need to further investigations of microwave imaging systems with more advanced breast phantoms. This will be a subject of our future research work.

VIII. Conclusion

The development of a multistatic UWB radar system for breast cancer detection has been presented. First, we have shown a novel hemispherical antenna array with sixteen UWB aperture stacked-patch antennas. The proposed system does not involve any mechanical scanning and provides a relatively fast measurement capability. The system was developed with the aim of future use in real clinical trials.

We use however the mechanical array rotation (angular rotation around the array center) to extract the tumor response from raw measured data. Therefore two scans (each 120 measurements) are required to obtain the 3D focused response.

Based on these two measurements we are able to subtract any undesired signals, e.g., direct antenna coupling, skin reflections and reflections from mechanical parts of the array.

The 3D images of scattered microwave energy within the breast volume are computed using post-reception focusing algorithms. We have presented and compared two algorithms: DAS and MAMI beamforming. Numerical simulations showed that with good preprocessing equalization of raw measured signals, MAMI provides better results in terms of signal-to-clutter ratio, compared with standard DAS. These findings were confirmed later by experimental results. Using a physical 3D curved breast phantom, we have experimentally demonstrated the ability to detect small (4 mm and 6 mm) tumors. Measured results show that in all experiments the signal-to-clutter ratio for MAMI is higher than for DAS. Experimental results agree qualitatively with findings from on numerical simulations.

As mentioned in the abstract, our radar system was designed to be used not only for laboratory experiments, but also for tests with real breast cancer patients. Preliminary results of the small clinical trial we have conducted is presented in [37].

References

[1] E. C. Fear, P. M. Meaney, and M. A. Stuchly, "Microwaves for breast cancer detection?," *IEEE Potentials*, vol. 22, no. 1, pp. 12–18, Feb.-Mar. 2003.

[2] P. M. Meaney, K. D. Paulsen, A. Hartov, and R. K. Crane, "Microwave imaging for tissue assessment: Initial evaluation in multitarget tissue-equivalent phantoms," *IEEE Trans. Biomed. Eng.*, vol. 43, pp. 878–890, Sep. 1996.

[3] P. M. Meaney, M. W. Fanning, D. Li, S. P. Poplack, and K. D. Paulsen, "A clinical prototype for active microwave imaging of the breast," *IEEE Trans. Microw. Theory Tech.*, vol. 48, pt. Part 1, pp. 1841–1853, Nov. 2000.

[4] P. M. Meaney, Q. Fang, Ch. A. Kogel, S. P. Poplack, P. A. Kaufman, and K. D. Paulsen, "Microwave imaging for neoadjuvant chemotherapy monitoring," presented at the Proc. 1st Eur. Conf. on Antennas Propag.: EuCAP, Nice, France, Nov. 6–10, 2006.

[5] S. P. Poplack, T. D. Tosteson, W. A. Wells, B. W. Pogue, P. M. Meaney, A. Hartov, C. A. Kogel, S. K. Soho, J. J. Gibson, and K. D. Paulsen, "Electromagnetic breast imaging: Results of a pilot study in women with abnormal mammograms," *Radiology*, vol. 243, no. 2, May 2007.

[6] R. Benjamin, "Synthetic, post-reception focusing in near-field radar," in *Proc. EUREL Int. Conf. on the Detection of Abandoned Land Mines: A Humanitarian Imperative Seeking a Tech. Solution*, Oct. 7–9, 1996, pp. 133–137.

[7] R. Benjamin, "Detecting reflective object in reflective medium," U.K. GB 2313969, Dec. 10, 1997.

[8] S. C. Hagness, A. Taflove, and J. E. Bridges, "Two-dimensional FDTD analysis of a pulsed microwave confocal system for breast cancer detection: Fixed-focus and antenna-array sensors," *IEEE Trans. Biomed. Eng.*, vol. 45, pp. 1470–1479, Dec. 1998.

[9] E. C. Fear, J. Sill, and M. A. Stuchly, "Experimental feasibility study of confocal microwave imaging for breast tumor detection," *IEEE Trans. Microw. Theory Tech.*, vol. 51, pp. 887–892, Mar. 2003.
[10] L. Xu, S. K. Davis, S. C. Hagness, D. W. van der Weide, and B. D. Van Veen, "Microwave imaging via space-time beamforming: Experimental investigation of tumor detection in multilayer breast phantoms," *IEEE Trans. Microw. Theory Tech.*, vol. 52, pt. Part 2, pp. 1856–1865, Aug. 2004.
[11] I. J. Craddock, R. Nilavalan, J. Leendertz, A. Preece, and R. Benjamin, "Experimental investigation of real aperture synthetically organized radar for breast cancer detection," in *Proc. IEEE Antennas Propag. Society Int. Symp.*, Jul. 3–8, 2005, vol. 1B, pp. 179–182.
[12] J. M. Sill and E. C. Fear, "Tissue sensing adaptive radar for breast cancer detection—experimental investigation of simple tumor models," *IEEE Trans. Microw. Theory Tech.*, vol. 53, pp. 3312–3319, Nov. 2005.
[13] R. Nilavalan, J. Leendertz, I. J. Craddock, R. Benjamin, and A. Preece, "Breast tumor detection using a flat 16 element array," in *Proc. 16th Int. Symp. on Electromagn. Compat. Topical Meeting on Biomed. EMC*, Zurich, Switzerland, Feb. 2005, pp. 81–84.
[14] R. Benjamin, G. Hilton, S. Litobarski, E. McCutcheon, and R. Nilavalan, "Post-detection synthetic near field focusing in radar or sonar," *Electron. Lett.*, vol. 35, no. 8, pp. 664–666, Apr. 1999.
[15] R. Benjamin, I. J. Craddock, G. S. Hilton, S. Litobarski, E. McCutcheon, R. Nilavalan, and G. N. Crisp, "Microwave detection of buried mines using non-contact, synthetic near-field focusing," *Proc. Inst. Elect. Eng. Radar, Sonar and Navigation*, vol. 148, no. 4, pp. 233–240, Aug. 2001.
[16] W. Zhisong, L. Jian, and W. Renbiao, "Time-delay- and time-reversal-based robust Capon beamformers for ultrasound imaging," *IEEE Trans. Med. Imaging*, vol. 24, pp. 1308–1322, Oct. 2005.
[17] E. C. Fear and M. A. Stuchly, "Microwave system for breast tumor detection," *IEEE Microw. Wireless Compon. Lett.*, vol. 9, pp. 470–472, Nov. 1999.
[18] E. J. Bond, L. Xu, S. C. Hagness, and B. D. Van Veen, "Microwave imaging via space-time beamforming for early detection of breast cancer," in *Proc. IEEE Int. Conf. on Acoust., Speech, and Signal Process. (ICASSP '02)*, May 13–17, 2002, vol. 3, pp. III-2909–III-2912.
[19] Y. Xie, B. Guo, L. Xu, J. Li, and P. Stoica, "Multi-static adaptive microwave imaging for early breast cancer detection," in *Proc. 39th Asilomar Conf. on Signals, Syst. and Comput.*, Nov. 1, 2005, pp. 285–289.
[20] Y. Xie, B. Guo, L. Xu, J. Li, and P. Stoica, "Multistatic adaptive microwave imaging for early breast cancer detection," *IEEE Trans. Biomed. Eng.*, vol. 53, pp. 1647–1657, Aug. 2006.
[21] R. Nilavalan, I. J. Craddock, A. Preece, J. Leendertz, and R. Benjamin, "Wideband microstrip patch antenna design for breast cancer tumor detection," *IET Microw., Antennas Propag.*, vol. 1, no. 2, pp. 277–281, Apr. 2007.
[22] I. J. Craddock, R. Nilavalan, A. Preece, J. Leendertz, and R. Benjamin, "Experimental investigation of real aperture synthetically organized radar for breast cancer detection," in *Proc. IEEE Antennas Propag. Society Int. Symp.*, 2005, vol. 1B, pp. 179–182.
[23] M. E. Hines and H. E. Stinehelfer, "Time-domain oscillographic microwave network analysis using frequency-domain data," *IEEE Trans. Microw. Theory Tech.*, vol. 22, pp. 276–282, Mar. 1974.
[24] P. Stoica, W. Zhisong, and L. Jian, "Robust Capon beamforming," *IEEE Signal Process. Lett.*, vol. 10, pp. 172–175, Jun. 2003.
[25] L. Jian, P. Stoica, and W. Zhisong, "On robust Capon beamforming and diagonal loading," *IEEE Trans. Signal Process.*, vol. 51, pp. 1702–1715, Jul. 2003.
[26] J. Leendertz, A. Preece, R. Nilavalan, I. J. Craddock, and R. Benjamin, "A liquid phantom medium for microwave breast imaging," presented at the 6th Int. Congress Eur. Bioelectromagn. Assoc., Budapest, Hungary, Nov. 2003.
[27] M. Lazebnik, L. McCartney, D. Popovic, C. B. Watkins, M. J. Lindstrom, J. Harter, S. Sewall, A. Magliocco, J. H. Booske, M. Okoniewski, and S. C. Hagness, "A large-scale study of the ultrawideband microwave dielectric properties of normal breast tissue obtained from reduction surgeries," *Phys. Med. Biol.*, vol. 52, pp. 2637–2656, 2007.
[28] W. Shao, B. Zhou, Z. Zheng, and G. Wang, "UWB microwave imaging for breast tumor detection in inhomogeneous tissue," in *Proc. IEEE-EMBS 27th Ann. Int. Conf. of the Eng. in Med. and Biol. Society*, 2005, pp. 1496–1499.
[29] L. Xu, E. J. Bond, B. D. Van Veen, and S. C. Hagness, "An overview of ultrawideband microwave imaging via space-time beamforming for early-stage breast-cancer detection," *IEEE Antennas Propag. Mag.*, vol. 47, no. 1, pp. 19–34, Feb. 2005.
[30] R. G. Lorenz and S. P. Boyd, "Robust minimum variance beamforming," *IEEE Trans. Signal Process.*, vol. 53, pp. 1684–1696, May 2005.
[31] R. A. Marr, U. H. W. Lammers, T. B. Hansen, T. J. Tanigawa, and R. V. McGahan, "Bistatic RCS calculations from cylindrical near-field measurements—Part II: Experiments," *IEEE Trans. Antennas Propag.*, vol. 54, pp. 3857–3864, Dec. 2006.
[32] I. J. LaHaie and M. A. Blischke, "Mitigation of multipath and ground interactions in RCS measurements using a single target translation," in *Proc. 23rd Ann. Meeting of Antenna Meas. Tech. Assoc. (AMTA 01)*, Denver, CO, 2001, pp. 411–416.
[33] M. A. Hernández-López, M. Quintillán-González, S. González García, A. Rubio Bretones, and R. Gómez Martín, "A rotating array of antennas for confocal microwave breast imaging," *Microw. Opt. Technol. Lett.*, vol. 39, no. 4, pp. 307–311, Nov. 2003.
[34] A. J. Surowiec, S. S. Stuchly, J. B. Barr, and A. Swarup, "Dielectric properties of breast carcinoma and the surrounding tissues," *IEEE Trans. Biomed. Eng.*, vol. 35, pp. 257–263, 1988.
[35] W. T. Joines, Y. Zhang, C. Li, and R. L. Jirtle, "The measured electrical properties of normal and malignant human tissues from 50 to 900 MHz," *Med. Phys.*, vol. 21, pp. 547–550, 1994.
[36] A. M. Campbell and D. V. Land, "Dielectric properties of female human breast tissue measured in vitro at 3.2 GHz," *Phy. Med. Biol.*, vol. 37, pp. 193–210, 1992.
[37] M. Klemm, I. Craddock, J. Leendertz, A. Preece, and R. Benjamin, "Experimental and clinical results of breast cancer detection using UWB microwave radar," presented at the IEEE Antennas and Propag. Society Int. Symp., San Diego, CA, Jul. 7–12, 2008.

Maciej Klemm was born in 1978. He received the M.Sc. degree in microwave engineering from Gdansk University of Technology, Poland, in 2002 and the Ph.D. degree from the Swiss Federal Institute of Technology (ETH) Zurich, Switzerland, in 2006.

In February 2003, he joined the Electronics Laboratory, ETH, where his research interests included small UWB antennas and UWB communications, antenna interactions with a human body, electromagnetic simulations, microwave MCM technologies, and millimeter-wave integrated passives (European IST LIPS project). In spring 2004, he was a Visiting Researcher at the Antennas and Propagation Laboratory, University of Aalborg, Denmark, where he was working on new antennas for UWB radios. In February 2006, he joined the University of Bristol (UoB), Bristol, U.K., where he currently holds the position of Research Associate. At UoB he is working on microwave breast cancer detection and UWB textile antennas. His involvement in the breast cancer project includes antenna design, electromagnetic modeling, experimental testing as well as participating in clinical trials.

Dr. Klemm received a Young Scientists Award in May 2004 at the IEEE MIKON Conference, for a paper about antennas for UWB wearable radios. He won the CST University Publication Award Competition in 2006 for a paper on the novel directional UWB antennas. In 2007 he won the "Set for Britain" competition for the Top Early-Career Research Engineer and received a Gold Medal at the Hose of Commons.

Ian J. Craddock is a Reader in the Centre for Communications Research, University of Bristol, Bristol, U.K. His research interests include antenna design, electromagnetics, biomedical imaging and radar, funded by organizations such as EPSRC, QinetiQ, DSTL and Nortel. He leads Bristol's breast cancer imaging project, which won the IET's Innovation in Electronics prize in 2006. He has published over 100 papers in refereed journals and proceedings. He has led a workpackage on ground-penetrating radar in an EU Network of Excellence and has a related active research interest in antennas and propagation for instrumentation within the human body. He has delivered numerous invited papers to conferences in Europe, the U.S. and Asia and chaired sessions at leading international conferences.

Jack A. Leendertz received the B.Sc. degree in physics with mathematics from Bristol University, Bristol, U.K.

He is currently engaged in electronics work at the University of Bristol. His research interests include microwave engineering, coherent optics in engineering, instrumentation for medical research and microwave imaging.

Alan Preece is a Clinical Scientist and Emeritus Professor of Medical Physics at Bristol University, Bristol, U.K. Previously, he researched biological effects of ionizing and nonionizing radiation on humans. His current work is applied to practical equipment design and the clinical application of microwave imaging in human subjects for the purpose of identifying and evaluating the imaging possibilities of such microwaves in detection of breast cancer.

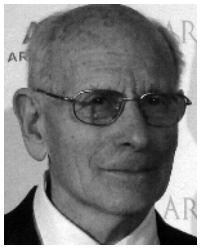

Ralph Benjamin received the B.Sc. degree in electronic engineering (1st class honors), the Ph.D. and the D.Sc. degrees from Imperial College, London, U.K.

He invented the single-sideband mixer during his undergraduate course, and joined RN Scientific Service in 1944. From 1947 to 1957, he developed the first countermeasure resistant 3D radar, and first force-wide integrated Command, Control, Communications and Intelligence System (CCIS). In 1947, he patented the interlaced cursor, controlled by joy-stick or mouse, to link displays to stored digital information. In 1947, he also patented the world's digital compression of video data, and first digital data link, still in use NATO-wide as "Link 11." From 1961 to 1964, he received repeated "special merit" promotions as Head of Research and Deputy Director, Admiralty Surface Weapons Establishment. He is the author of the textbook on *Signal Processing* and the 1961 Acting International Chairman NATO "Von Karman" studies on "Man and Machine" and "Command and Control." In the 1950s and 1960s, he was a Leading member of the DTI Advanced Computer Techniques Project, from 1964 to 1971, he was Chief Scientist Admiralty Underwater Weapons Establishment (AUWE), and from 1965 to 1971, Director, AUWE, and MoD Director Underwater Weapons R&D (and member of Navy Weapons Department Board). From 1971 to 1982, he was Chief Scientist, Chief Engineer, and Superintending Director, GCHQ. This entailed responsibility for fast-track research, development, procurement, and deployment and use of equipment and techniques for the collection, interpretation, evaluation, and assessment of electronic or signals intelligence information. (Most projects had to create urgent solutions to problems which the opposition's leading experts thought they had made impossible.) From 1972 to 1982, his functions were combined with those of Chief Scientific Advisor to both the Security Service and SIS, and with acting as Cabinet Office Coordinator, Intelligence R&D. From 1972 to 1978, he was a visiting Professor at the University of Surrey for two three-year terms, during which time he helped to start the Surrey University mini-satellite program. From 1982 to 1987, he was Head of Communications Techniques and Networks and semi-official Global Research Coordinator NATO (SHAPE Tech Centre). Graduate NATO Staff College, 1983. During all these appointments, he combined the administration of large scientific/engineering organizations and of their R&D programs, with creative, innovative up-front leadership, as illustrated by numerous classified and Learned-Society publications and patents. Currently, he is a Visiting Research Professor, University College, London, and Bristol University, Bristol, U.K. Until recently, he was also a Visiting Professor at Imperial College, London, U.K., External Ph.D. Supervisor, Open University, external Post-Graduate Course Examiner, Military College of Science, and Member of Court, Brunel University.